EUROPEAN JOURNAL OF MATERIALS SCIENCE AND ENGINEERING
Volume 11, Issue 3, 2026: 239-254 | www.ejmse.ro | ISSN: 2537-4338

DOI: 10.36868/ejmse.2026.11.03.239

EVOLUTION OF MICROSTRUCTURE AND MECHANICAL PERFORMANCE OF TIG-WELDED AA6061–AA6063 JOINTS: INFLUENCE OF JOINT CONFIGURATION AND HEAT INPUT

Augustine B. OKOUBULU[1,2][0009-0006-1681-3067], Akeem M. AJAO[2][0009-0002-5175-6564], Cynthia C. NWAEJU-OKECHUKWU[3,4*][0000-0001-6796-3651], Henry E. MGBEMERE[2][0000-0003-3887-7628]

[1]Materials and Metallurgical Engineering Department, Southern Delta University, P.M.B. 5, Ozoro, Nigeria
[2]Metallurgical and Materials Engineering Department, University of Lagos, Akoka-Yaba, Lagos, Nigeria
[3]Department of Mechanical Engineering, Nigeria Maritime University, Okerenkoko, Delta State, Nigeria
[4]Department of Metallurgical and Materials Engineering, Nnamdi Azikiwe University, P.M.B. 5025 Awka.

Abstract

Dissimilar aluminium alloys are widely used in automotive and aerospace structures because they are lightweight and strong. However, joining these alloys by fusion welding remains challenging because their different chemical compositions and thermal behaviour strongly affect weld quality. This study investigates how joint configuration and heat input influence the microstructure, phase stability, and mechanical performance of TIG-welded AA6061-AA6063 joints. Plates of AA6061 and AA6063 were welded using 4043 filler metal in single-V, half-V, double-V, lap, and no-joint configurations, with welding currents ranging from 110 to 130 A. Mechanical testing (tensile strength, hardness, impact), SEM/EDS, XRD, and spectrometric analysis were conducted to evaluate changes induced by welding conditions. The weld metal showed reduced aluminium content and significant increases in silicon, magnesium, and copper due to dilution with the 4043 filler. Heat input and joint configuration substantially influenced hardness and toughness. Quantitative evaluation showed that a half-V configuration at 130 A achieved the highest hardness (150.63 HV), while the double-V configuration at 130 A delivered the highest impact energy (41.34 J). The single-V configuration at 130 A produced the maximum tensile strength (98.7 MPa) with 19.6% elongation. SEM/EDS analysis revealed increased pore density with rising heat input, which was suspected to be due to higher gas entrapment during solidification. XRD showed no major phase transformations across the joint designs, suggesting that mechanical variations were primarily governed by microstructural refinement and elemental redistribution rather than the formation of new phases. These findings provide novel insight into the optimization of TIG welding parameters for dissimilar 6xxx-series aluminium alloys, providing practical guidance for lightweight structural applications.

Keywords: *Dissimilar aluminium alloys, TIG welding, joint configuration, heat input, microstructure, mechanical properties.*

Introduction

Aluminium alloys remain important engineering materials since they are lightweight, strong, resist corrosion and can be easily shaped. These properties make them suitable for aerospace, automotive, marine, and other engineering applications [1]. More than 300 aluminium alloy grades are commercially available, and many are optimized for specific mechanical and service requirements through controlled additions of silicon, magnesium, copper, or manganese [1]. Among these alloys, the heat-treatable 6xxx-series, especially AA6061 and AA6063, are widely used in transportation because they are strong, weldable, and easy to extrude [2].

*Corresponding author: cynthianwaeju@gmail.com;

In modern vehicle and aircraft manufacturing, parts with the same design are often produced from dissimilar aluminium alloys to reduce weight, lower costs, and ease forming [3]. This makes fusion welding essential during assembly, particularly when joining different aluminium alloys on the same structural platform. However, welding aluminium is difficult because of its high thermal conductivity, stable oxide film, hydrogen solubility, and susceptibility to defects such as pores and cracks [3]. These challenges intensify when joining dissimilar alloys because of differences in melting temperatures, thermal expansion, and solute compositions, which affect the weld pool and final microstructure [4], [5].

TIG welding is preferred for aluminium because it provides a stable arc, clean welds, and precise heat control, yielding strong, reliable joints when process parameters are optimized [6]. However, weld quality in TIG welding is strongly influenced by heat input, joint geometry, welding current, and filler metal composition [7], [8], [9]. Heat input primarily determines weld bead shape, microstructural changes, HAZ softening, dissolution of strengthening precipitates, and the formation of solidification defects [10], [11]. Similarly, joint configuration controls weld penetration, filler distribution, cooling rate, and weld metal morphology, especially in thick or dissimilar joints [12], [13].

AA6061 and AA6063 differ in magnesium-silicon (Mg-Si) ratios and strengthening effects, resulting in distinct melting properties, hardness profiles, and precipitation characteristics [14]. Welding these alloys together typically induces phase transformations, solute redistribution, and a non-uniform microstructure due to compositional differences and heat transfer [15], [16]. These microstructural changes control joint strength, hardness, fracture behaviour, and phase stability, making it important to examine how welding parameters and joint design affect these properties.

Although several studies have examined TIG welding of similar aluminium alloys individually, research on the combined effects of heat input, joint configuration, and filler composition on dissimilar AA6061-AA6063 joints remains limited. Most available studies focus on welding similar alloys, laser welding, or friction-based joining processes, leaving a gap in understanding of fusion-welded dissimilar 6xxx-series aluminium joints [17], [18], [19]. This work is novel in that it quantitatively demonstrates how joint design and heat input jointly control microstructural refinement, elemental redistribution, and mechanical performance. This knowledge gap is significant because the automotive and structural industries increasingly use mixed-alloy systems and require reliable guidelines for selecting welding parameters for dissimilar aluminium systems.

Therefore, this study investigates the microstructural evolution, phase stability, and mechanical performance of TIG-welded AA6061-AA6063 dissimilar joints produced under different joint designs and heat inputs. By combining mechanical testing, SEM/EDS, XRD analysis, and compositional evaluation, the study provides insight into how joint design or configuration choices influence microstructure, strength, porosity, and phase formation in these widely used aluminium alloys. The findings contribute to establishing optimized TIG welding parameters for dissimilar aluminium alloy joints and aid better manufacturing design in automotive and structural applications.

Materials and Methods

Materials

Two wrought aluminium alloys commonly used in automotive applications, AA6061 and AA6063, were selected for this study. The AA6061 plates were sourced from the open market, whereas the AA6063 alloy was obtained from Nigalex Aluminium Company. Filler metal ER4043, containing approximately 5% Si, was used for its well-established compatibility with 6xxx-series alloys and its ability to reduce susceptibility to hot cracking during welding [20]. High-purity argon (99.99%) served as the shielding gas throughout the TIG welding process. As shown in Fig. 1, both alloys were cut into 100 mm × 50 mm coupons prior to welding to obtain the required material size.

The AA6063 bar was melted and recast into flat sheets to match the geometry of the AA6061 plates. The chemical composition of the filler metal and the AA6061 and AA6063 base materials is listed in Table 1.

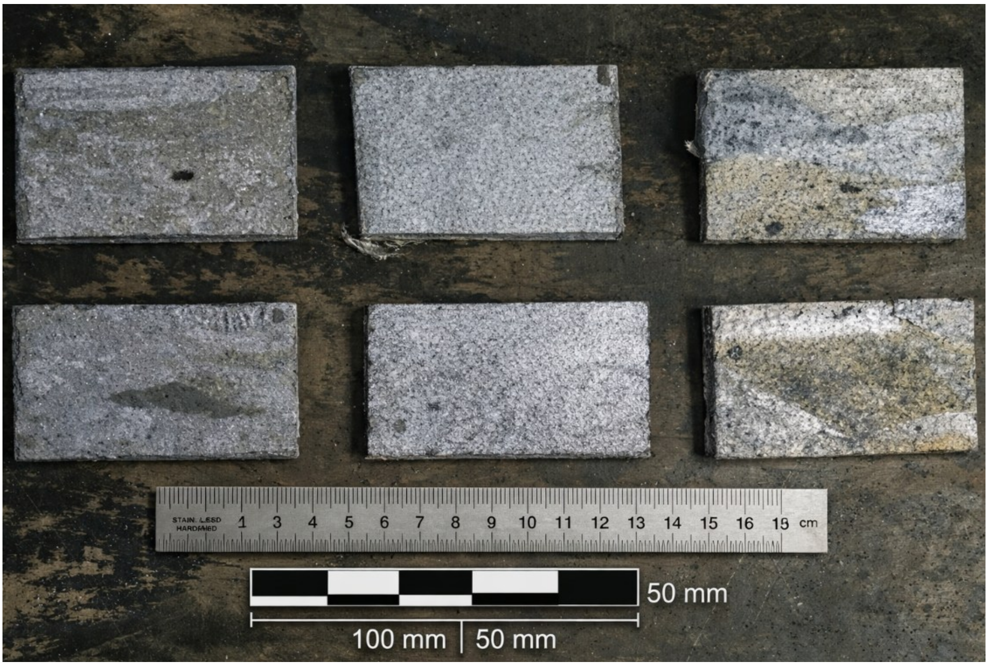

Fig. 1. Base material sample size

Table 1. Chemical Composition of the filler metal and the base materials (wt.%)

	Al	Si	Fe	Cu	Mn	Mg	Zn	Cr	Ni	Ti
AA6061 Plate	Bal	0.14	0.11	2.15	0.52	0.80	0.02	0.02	0.12	-
AA6063 Bar	Bal	0.54	0.33	0.07	0.04	0.28	0.09	0.02	0.09	-
Filler metal ER4043	Bal	4.6	0.79	0.28	0.05	0.04	0.09	-	-	0.2

Experimental Details

Five joint configurations were prepared to evaluate the influence of joint design on weld quality and heat input: single V-configuration (V1), half V-configuration (V1/2), double V-configuration (V2), no-joint configuration (NC), and lap joint (L) configuration (see Fig. 2). The joint configurations were produced manually with a hacksaw, followed by filing to ensure uniformity. Joint geometry is known to influence weld penetration, porosity formation, and fusion zone morphology [21], [22]. Welding was carried out using a conventional TIG (GTAW) setup under a shielding environment of commercially pure argon. A tungsten non-consumable electrode was employed to produce the arc, and the argon shielding protected the aluminium against oxidation and hydrogen absorption, which are major considerations during aluminium welding [23]. The welding variables of voltage, arc length, and tungsten tip profile remained constant during the welding process. Welding was performed in four passes for each joint configuration. For each joint design, five test samples were welded at three different welding currents (110 A, 120 A, and 130 A). Some of the welded specimens are shown in Fig. 3. The welding parameters used for the passes are presented in Table 2. Details of the welding current, voltage, travel speed, heat input for each pass, and the overall heat input, calculated assuming a thermal efficiency of 60% for the GTAW process, are also provided in Table 1.

The thermal cycle of the welding process is strongly influenced by heat input [24]. Heat input is the energy supplied during welding and is governed by the welding current, voltage, and travel speed. In this study, heat input was calculated using the ASME Section IX standard equation (1):

$$Heat\ Input\ (kJ/mm) = (V\ x\ I\ x\ 60)/(1000\ x\ S) \quad (1)$$

Where: V = voltage (kept at 230 V), I = current (A), S = travel speed (mm/min).

Table 2. Chemical Composition of the filler metal and the base materials (wt.%)

Joint Design	Current (Amps)	Time (sec)	Speed (mm/min)	Heat input (kJ/mm)	Total heat input, kJ/mm
V 1/2	110	42	142.8	10.63	160.95
V 1/2	120	45	133.2	12.43	
V 1/2	130	32	187.8	9.55	
V 1	110	52	115.2	13.18	
V 1	120	46	130.2	12.72	
V 1	130	42	142.8	12.56	
V 2	110	85	141.0	10.77	
V 2	120	70	171.6	9.65	
V 2	130	71	168.6	10.64	
L	110	93	129.0	11.77	
L	120	77	156.0	10.62	
L	130	78	153.6	11.68	
NC	110	41	146.4	10.37	
NC	120	52	115.2	14.38	

(a) Single-V Joint Configuration

(b) Half-V Joint Configuration

(c) Double-V Joint Configuration

(d) Lap Joint Configuration

(e) No Joint Configuration Butt Joint

Fig. 2. Showing the various Weld Joint Configurations

Fig. 3. Welded Joints

Characterization and Mechanical

Spectrometry analysis was carried out to identify the specific elemental composition of the base materials and the welded joints. The chemical composition analysis was conducted using an Optical Emission Spectrometer (OES) (AMETEK Materials Division, Kleve, Germany) for the base materials, filler material, and welded material. The compositions of the base metal and the weld metal were compared to assess changes introduced by the welding process, including elemental segregation, dilution effects, and the potential loss of volatile constituents.

The specimens were prepared by successive mechanical grinding with SiC abrasive papers ranging from 80 to 2000 grit, followed by polishing with a 1 µm alumina slurry. After polishing, the mirror-polished specimens were etched with Keller's reagent (190 mL distilled water, 5 mL nitric acid, 3 mL HCl, and 2 mL HF) for 20-25 seconds to reveal the microstructure in the weld fusion zone (WFZ). X-ray diffraction (XRD) analysis was used for phase identification and to detect phase changes caused by varying heat input. XRD helps confirm solute redistribution and the formation of Mg_2Si and other strengthening phases in 6xxx-series aluminium alloys [25]. The XRD measurements were conducted using an Empyrean diffractometer (Malvern Panalytical, Almelo, Netherlands) equipped with Ni-filtered Cu Kα radiation.

The specimens for the tensile test were prepared to the dimensions specified in ASTM E8M. The tensile test was performed at room temperature in accordance with ASTM E8 at a rate of 1 mm/min using a universal testing machine (Model: TENSLON RTF Series, A&D Company, Tokyo, Japan) with a 50 kN load capacity. The impact test was conducted using an Instron Charpy Impact Testing Machine (Model: CEAST 9050 Pendulum Impact Tester, Instron, Norwood, USA). The Charpy V-notch impact toughness test was carried out on sub-size specimens measuring 55 mm x 10 mm x 7.5 mm. Microhardness measurements were carried out with a Micro-Vickers hardness tester (HMV Series, Shimadzu Corporation, Kyoto, Japan) under a load of 500 g and a dwell time of 10 s. For each property test, three specimens were evaluated, and the average values were reported. Scanning electron microscopy (SEM) was carried out using a Zeiss Sigma equipped with an Oxford Instruments X-Max 80mm silicon drift detector (SDD) for EDS analysis.

Test Results and Discussion

Chemical Composition

The chemical compositions of the base metals, filler material, and welded metal were measured by an Optical Emission Spectrometer (OES) (AMETEK Materials Division, Kleve, Germany), as shown in Table 1 below. The results showed that the AA6061 plate consisted primarily of aluminium (95.63%), with notable additions of copper (2.15%), magnesium (0.80%), and manganese (0.52%), along with minor silicon (0.14%) and iron (0.11%). AA6063 had a higher aluminium content (97.88%) with lower alloying elements, especially copper (0.07%) and magnesium (0.28%). These results align with standard alloy designations, in which AA6061 prioritizes strength, and AA6063 prioritizes ductility and formability [26]. The filler metal ER4043 is Si-rich (4.6%).

The post-weld chemical compositions of the base and weld metals were also measured, as shown in Table 2. The results indicate that, except for Si, most elemental concentrations in the weld metal are lower than in both the base and filler metals, likely due to high-temperature evaporation, burn-off, and oxidation during welding. In contrast, the Si content increases relative to the base metal because the 4043 filler is Si-rich. The weld joint showed reduced aluminium (89.95%) and increased silicon (6.80%), copper (2.03%), and magnesium (0.69%) levels (see Table 2). These changes reflect the use of the Al 4043 filler, which contains ~5% silicon to enhance fluidity and wetting during welding. This composition promotes improved fusion and strengthening of the weld zone [2]. The redistribution of alloying elements underscores the importance of filler metal selection and controlled heat input in TIG welding. These changes affect microstructure and mechanical performance, consistent with the findings of Karthick et al. and Alzahrani et al. [27], [28].

Table 3. Post weld Chemical Composition of the base materials and weld metal (wt.%)

	Al	Si	Fe	Cu	Mn	Mg	Zn	Cr	Ni	Ti
AA6061-AA6063 Joint	Bal	6.80	0.10	2.03	0.37	0.69	0.01	0.01	0.02	0.02
AA6063 Post weld	Bal	1.99	0.53	0.07	0.05	0.45	0.11	0.02	0.01	0.02
AA6061 Post weld	Bal	0.48	0.18	4.48	0.05	0.04	0.02	0.02	0.01	0.04

Microhardness Distribution

The microhardness chart shown in Fig. 4 presents the Vickers microhardness (HV) values for AA6061 and AA6063 alloys and their fusion zones across various joint configurations and welding currents. The Fig. shows variation in hardness across different regions of the welded joints.

In AA6061 alloy, hardness generally ranges from 112.63HV (V1/2 configuration at 110A) to 150.63 HV (V1/2 configuration at 130A). This indicates that the welding current strongly influences the hardness of the AA6061 base metal, with higher currents producing greater hardness. The AA6063 alloy exhibits hardness values ranging from 55.17 HV to 87.9 HV. The peak hardness for AA6063 occurs in the L130 configuration (lap joint at 130A).

The fusion zone (where the two dissimilar alloys and filler metal mix) exhibits hardness values ranging from 61.97 HV to 93.47 HV. The peak hardness in the fusion zone occurs in the V2 130 configuration (double-V-configuration at 130 A). Increased welding current generally improves hardness by enhancing fusion and refining the microstructure. This is evident in the AA6061 alloy, where hardness increases from 110 A to 130 A with the V1/2 configuration. Similarly, the fusion zone shows its highest hardness at 130A (V2 130). The double-V configuration (V2) consistently yields higher hardness, attributable to improved penetration and uniform heat distribution. This pattern is observed in the fusion zone, where V2 130 shows the highest hardness. The findings show that both the joint configuration and welding current play significant roles in determining the microhardness of the welded joint. Different combinations of these parameters lead to varying hardness profiles across the base metals and the fusion zone. The microhardness results align with existing literature (Khalfallah et al., Shafeek et al., and Bansal et al.) that emphasizes the importance of heat input, filler composition, and cooling rate in influencing weld hardness [29], [30], [31].

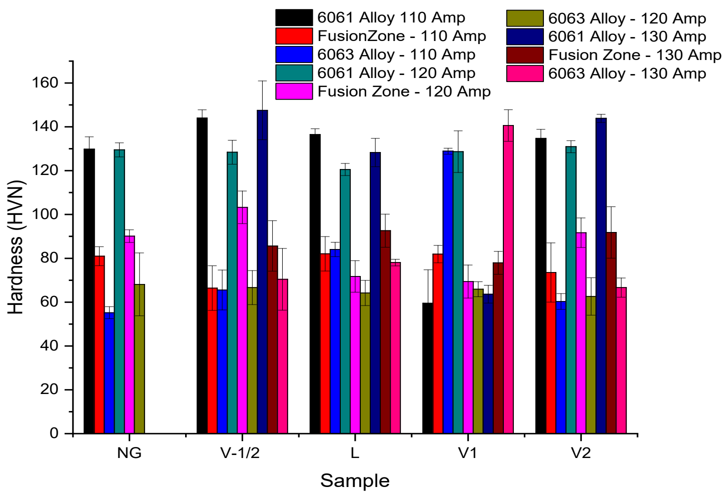

Fig. 4. Microhardness distribution across base metals and fusion zones for all joint configurations

Tensile Strength

V1 Configuration Performance

V1 at 130 A achieved the highest ultimate tensile strength (UTS) of approximately 98.7 MPa and an elongation of about 19.6%. This demonstrates superior tensile performance in the single-V-configuration. Improved heat input promotes interfacial bonding and reduces defects, leading to an optimal combination of strength and ductility.

Fig. 5 shows the V1 configuration (single-V configuration). The curve indicates that V1-110A and V1-120A have lower UTS and elongation than VI-130A. The higher heat input (130 A) for the V1 configuration appears to improve interfacial bonding and reduce defects, resulting in higher tensile strength and ductility.

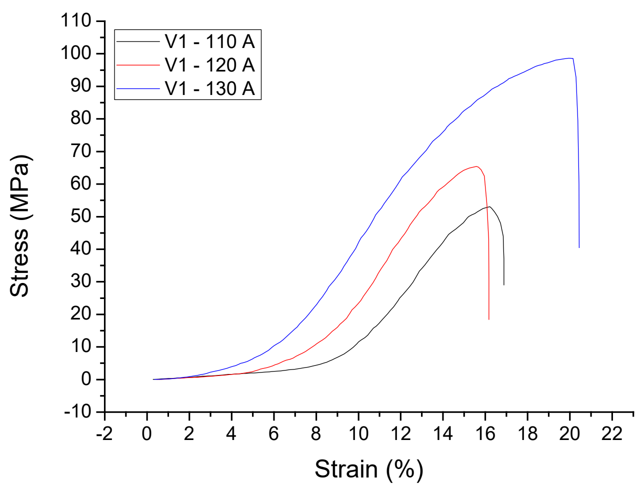

Fig. 5. Tensile stress-strain curves for V1 configuration at different currents

V2 Configuration Performance

V2 at 110 A exhibited the highest ultimate tensile strength (UTS) of approximately 72 MPa at 12% strain, whereas V2 at 120 A and 130 A showed lower UTS and ductility. The lower performance of V2-130A could be attributed to grain coarsening caused by higher heat input. This indicates that for the V2 configuration, excessive heat input (130 A) can be detrimental to tensile properties, whereas for the V1 configuration, it is not. Fig. 6 shows the performance of the V2 joint configuration.

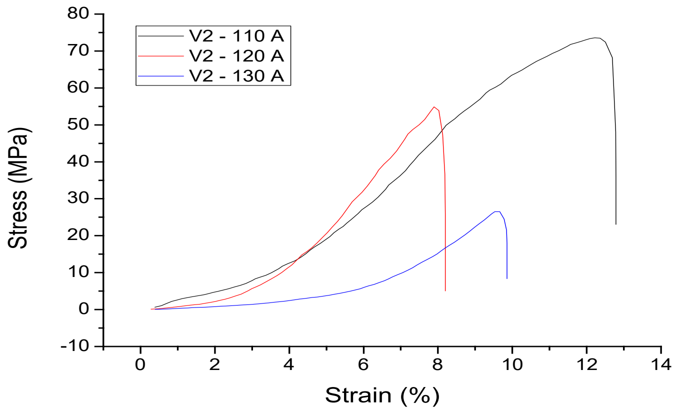

Fig. 6. Tensile stress-strain curves for V2 configuration at different currents

V1/2 Configuration Performance

V1/2 at 120 A showed an optimal tensile strength of approximately 93 MPa and ductility as illustrated in Fig. 7. This finding highlights the importance of combining an appropriate joint configuration with a suitable heat input. V1/2 configuration, 120 A appears to be the optimal current, balancing strength and ductility.

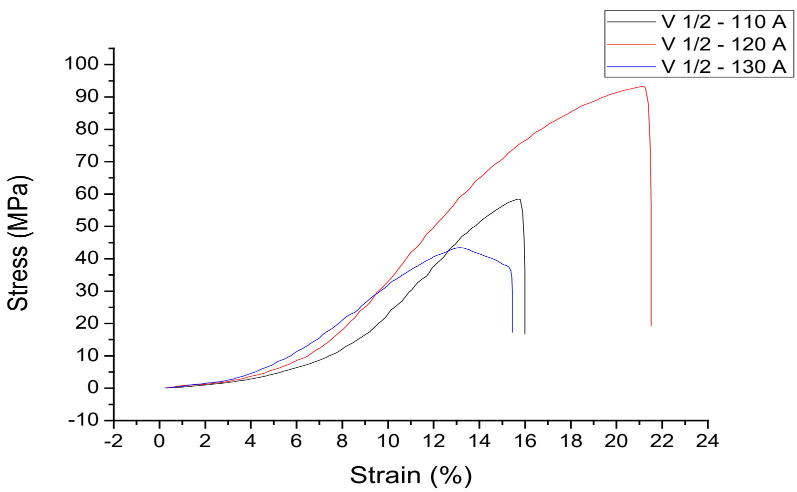

Fig. 7. Tensile stress-strain curves for V1/2 configuration at different currents

L and NC configuration (Lap and No-Configuration)

L at 130A showed an improved UTS of approximately 72 MPa and a ductility of 3% strain compared with the other L configuration. The lap and no-joint configuration is shown in Fig. 8.

NG at 110A recorded the lowest UTS, approximately 36 MPa. These findings confirm the significant role of joint preparation.

The no-configuration design, with inadequate joint preparation, produced significantly lower tensile strength, likely due to poor penetration and incomplete fusion. The lap joint, while better than a no-joint configuration, still exhibits lower ductility than that of optimized V-joint designs.

This work also shows that no single parameter is best; rather, superior tensile properties require an optimal combination of heat input and joint geometry. For example, V1/2-120A and V1-130A exhibited high tensile strength, whereas V2-110A was optimal for the double-V configuration. The contrasting behaviour of V1-130A (improved performance) and V2-130A (reduced performance due to grain coarsening) at higher heat input highlights the sensitivity of different joint geometries to welding current. Optimal parameters yield defect-free, ductile welds, but insufficient or excessive heat compromises mechanical integrity [11], [31].

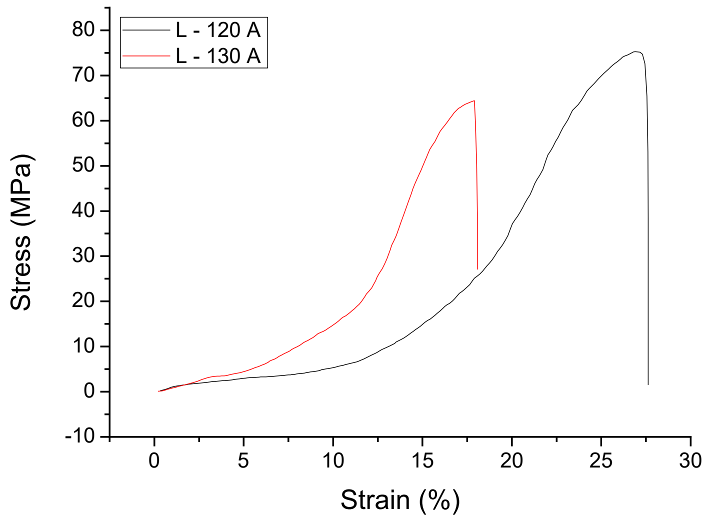

Fig. 8. Tensile stress-strain curves for L configuration at different currents

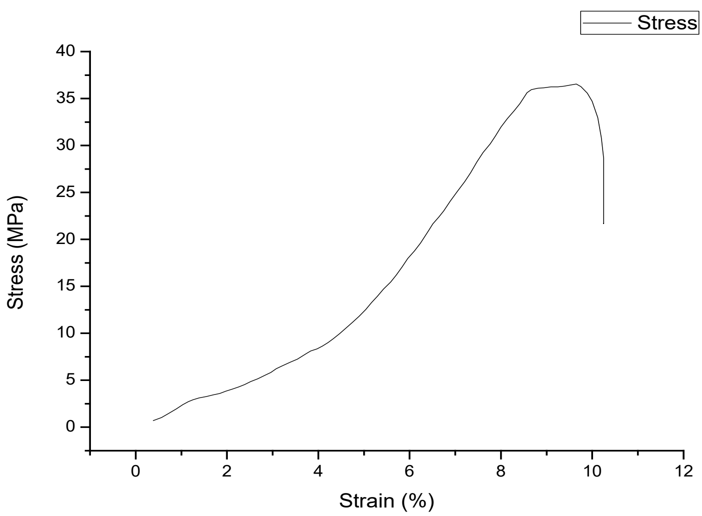

Fig. 9. Tensile stress-strain curves for No-Configuration design

Microstructural Characterization

SEM/EDS Analysis

The microstructural characteristics and elemental composition of the welded AA6061-AA6063 joints, particularly focusing on the V2 configuration samples at different welding currents of 110 A, 120 A, and 130 A is shown in Fig. 10. The SEM micrographs for V2 at 110 A showed uniform, refined grains. This demonstrates that lower heat input promote a finer microstructure which generally enhanced mechanical performance. While V2 at 130 A displayed larger grains and porosity as shown in Fig. 10(c). The increased heat input (high current) lead to grain coarsening and greater gas entrapment during solidification bringing about higher pore density. Coarse grains and porosity reduce ductility and toughness. The microstructure is strongly determined by welding parameters and joint design. Coarse grains or voids negatively impact toughness and ductility while fine, uniform grains improved mechanical performance. These results are consistent with previous studies by Yang et al. and Dak & Pandey [32], [33].

Elemental Distribution

EDS confirmed aluminium dominance in the weld samples and main alloying elements were magnesium (Mg), silicon (Si), chromium (Cr), and Nickel (Ni). Other elements such as oxygen (O), calcium (Ca) and phosphorous (P) were seen to be present in very small quantity. The presence and distribution of alloying elements are important for the improved mechanical properties of the weld. The EDS confirms their incorporation into the weld metal.

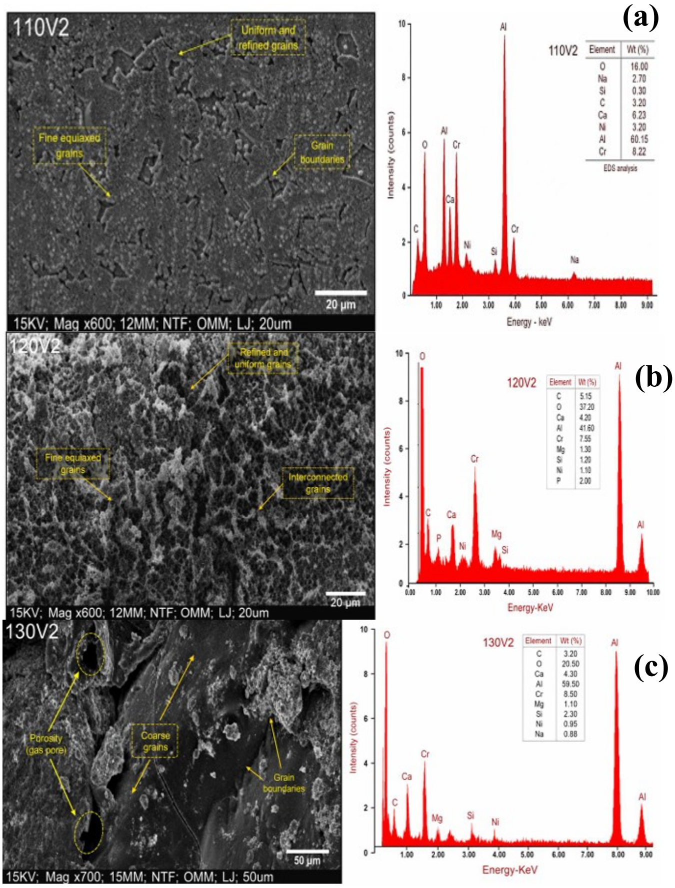

Fig. 10. SEM micrographs and EDS spectra for samples (a) V2 at 110 A, (b) V2 at 120 A, and (c) V2 at 130 A.

Phase Analysis (X-ray Diffraction)

The X-ray diffraction results in Fig. 11 provide information on phase stability and crystallographic features of the TIG-welded dissimilar AA6061-AA6063 joints, focusing on V2 configuration samples at welding currents of 110 A, 120 A, and 130 A. The primary finding from the XRD patterns is the presence of a stable crystalline phase across the V2 configuration at the different welding currents. This indicates that the welding process, using the V2 joint design and the investigated heat input, did not introduce any major undesirable phase transformations. This is a positive result, as the formation of unstable phases can severely compromise the mechanical integrity and long-term performance of welded joints. While the phases remained stable, the XRD patterns showed variations in intensity. These variations are due to differences in crystallographic orientation and grain size among the samples. The observed variations in mechanical properties, such as tensile strength, hardness, and impact toughness, are primarily driven by microstructural evolution (e.g., grain coarsening, grain refinement, and elemental distribution) rather than by the formation of new phases [34], [35].In the event of i = 2, this process enables the combination of two equations, thus facilitating the validation of the model illustrated in Fig. 4. This Fig. demonstrates the evolution of the relaxation modulus, obtained with respect to the experimental points. A strong correlation is evident between the predicted data and the experimental points. The mean relative error between the analytic model's prediction and the experimental points is approximately 3.93%. However, this discrepancy could be linked to measurement errors, the construction of the master relaxation curve, as well as the non-uniqueness of the parameter identification response.

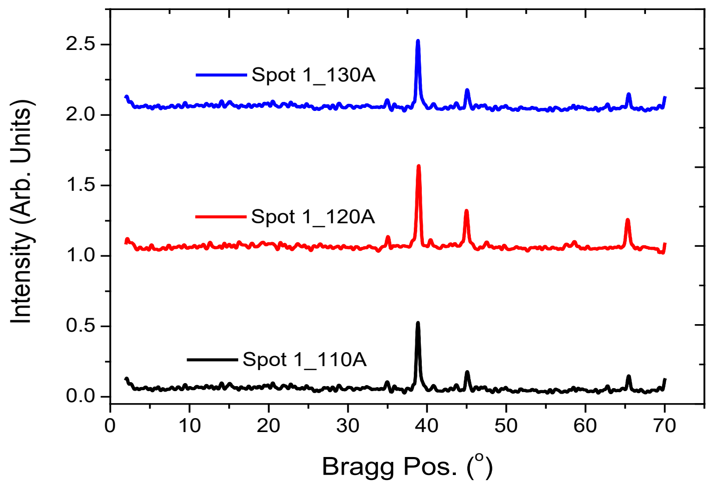

Fig. 11. XRD patterns of V2 configuration weld bead at 110 A, 120 A, and 130 A

Impact Toughness

The impact toughness results show a clear relationship among joint configuration, heat input, and the welded joint's energy absorption before fracture. V2 at 130 A exhibited the highest impact toughness, 41.34 J. This finding indicates that this combination of heat input and joint geometry is optimal for maximizing the energy absorption capacity of dissimilar AA6061-A6063 joints. V2 at 120 A showed a slight decrease in impact energy compared to V2 at 130 A. This could be attributed to local microstructural anomalies, suggesting that even small differences in welding parameters can affect material properties. Optimized heat input and joint configuration improve toughness by promoting a refined, uniform microstructure [32], [36].

The impact toughness results reveal that for TIG-welded dissimilar AA6061-AA6063 joints, a double-V configuration (V2) combined with a higher (but not necessarily the highest) heat input (130A in this study) can lead to superior toughness.

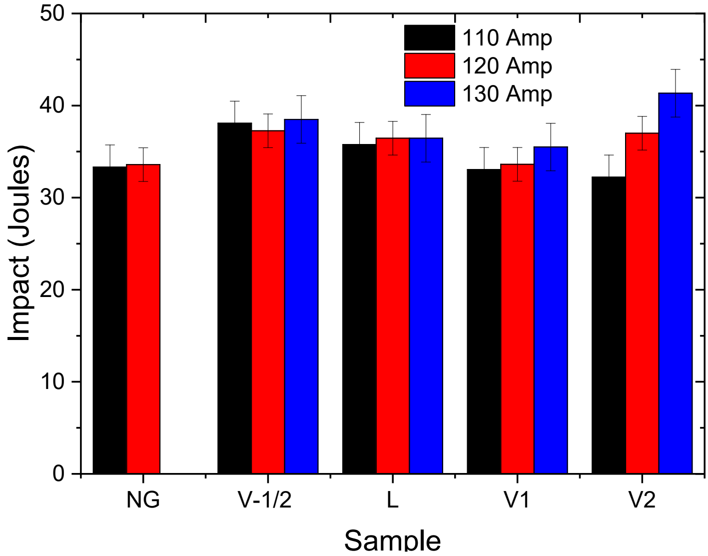

Fig. 12. Impact energy of welded samples versus joint configuration and heat input

Correlation of Microstructure, Mechanical Properties and Welding Parameters

The study establishes the following correlations:

(a) Heat Input and Mechanical Properties via Grain Refinement and Fusion Quality. Heat input directly determines hardness, tensile strength, and impact toughness. This control is primarily achieved through its influence on grain refinement and fusion quality. Optimal heat input promotes finer grains in the weld metal. Finer grains increase hardness and strength due to the Hall-Petch effect. Adequate heat input ensures proper melting and mixing of the filler material and base metals, resulting in good fusion and minimizing defects such as lack of fusion. Both insufficient and excessive heat input can be detrimental. Excessive heat leads to grain coarsening (reducing toughness and strength) and increased porosity (as observed in SEM/EDS analysis), while insufficient heat can cause poor fusion [37].

(b) Joint Configuration and Mechanical Integrity via Penetration and Fusion Uniformity

Joint configuration governs penetration, fusion uniformity, and mechanical integrity. The V2 and V1/2 configurations consistently showed better results across various mechanical tests, including tensile strength, hardness, and toughness.

Appropriate joint design enables deeper, more consistent weld penetration into the base metals, ensuring a strong bond. Well-designed configurations promote uniform distribution of the molten metal and filler, yielding a more homogeneous weld bead and reducing stress concentrations. The no-joint configuration (NC) designs perform poorly due to inadequate penetration and incomplete fusion, underscoring the importance of proper joint preparation.

(c) Microstructure and Mechanical Performance via Grain Structure and Elemental Distribution.

The microstructure and elemental distribution directly determine mechanical performance. Uniform, refined grains enhance strength and ductility, whereas porosity or coarse grains reduce strength and toughness. Fine grains improve strength and toughness. Coarse grains, usually caused by high heat input and slow cooling, provide fewer grain boundaries to hinder dislocation movement, thereby lowering strength and ductility.

The compositional analysis (SEM/EDS) showed elemental redistribution caused by the 4043 filler metal, with increased Si, Cu, and Mg in the weld metal. When uniformly distributed, alloying elements improve strength and other mechanical properties. A non-uniform distribution leads to localized weak spots. The XRD results revealed that mechanical variations were mainly due to microstructural refinement and elemental redistribution, not the formation of new phases. The findings are consistent with previous studies and confirm that optimal welding parameters ensure a strong, ductile, and tough dissimilar joint [35], [36], [38].

Conclusion

The comprehensive investigation of TIG-welded AA6061-AA6063 dissimilar joints under variable joint configurations and heat inputs leads to the following conclusions:

1. Joint configuration significantly affects weld quality. V2 and V1/2 geometries consistently outperformed L, V1, and NG in terms of hardness, tensile strength, and toughness. No-joint configuration performed poorly due to inadequate penetration and incomplete fusion.
2. Heat input directly influences mechanical properties. Optimal heat input enhances tensile strength, hardness, and ductility, while excessive or insufficient heat leads to grain coarsening, porosity, or weak fusion zones.
3. Microstructural evolution is critical. Refined grains in the fusion zone enhance strength and toughness, whereas coarse grains or voids degrade mechanical behaviour. SEM/EDS analysis confirms the crucial role of alloying elements and filler composition in determining the microstructure.
4. Phase stability is maintained across welding conditions. XRD analysis confirmed the presence of stable crystalline phases and the absence of deleterious phases, indicating that mechanical performance is governed by microstructural quality rather than by phase transformation.
5. Optimal welding parameters are essential for performance. Carefully controlled joint geometry and heat input can produce dissimilar aluminium welds with superior mechanical and microstructural properties suitable for structural and engineering applications.

Future developments will focus on extending the proposed methodology to coupled hygro-thermo-mechanical loading, where moisture diffusion and temperature significantly affect the viscoelastic response of natural fibres. Additional investigations will also address the evolution of the relaxation spectrum during ageing, fatigue and environmental degradation, as well as comparisons with fractional viscoelastic models and data-driven identification techniques. These perspectives will contribute to establishing reliable predictive tools for lifetime assessment and structural design of sustainable bio-composite materials.

Overall, this study demonstrates that the continuous spectrum of relaxation times is not merely an alternative mathematical representation of viscoelasticity but a powerful physical modelling framework capable of linking the hierarchical microstructure of kenaf bast fibres to their long-term mechanical behaviour. It therefore provides a significant step towards the development of robust, physically based constitutive models for natural fibres and their structural composite applications.

Acknowledgments

The authors would like to acknowledge that AI tools was used only for minor language editing and grammar improvement during the manuscript preparation. All experimental work, results, analyses, and interpretations presented in the manuscript are entirely original and were carried out by the authors

References

[1] R. Yadav, V. K. Dwivedi, and S. P. Dwivedi, "Analysis of mechanical properties and manufacturing process of aluminum series," *J. Inst. Eng. Ser. D*, pp. 1–13, 2024.

[2] A. Nasi, K. Dhoska, A. Sulejmani, K. Koka, and O. Koça, "Comprehensive Analysis of 6061 and 6063 Aluminum Alloys: Applications and Mechanical Properties," in *International Conference on Intelligence-Based Transformations of Technology and Business Trends*, Springer, 2025, pp. 158–167.

[3] M. F. Jamaludin, A. B. Abdullah, Z. Samad, and F. Yusof, "Formability analysis of dissimilar aluminium tailor welded blanks by low-powered fibre laser for lightweight automotive application," *J. Appl. Eng. Des. Simul.*, vol. 5, no. 1, pp. 57–65, 2025.

[4] E. Schubert, "Challenges in thermal welding of aluminium alloys," *World J. Eng. Technol.*, vol. 6, no. 02, pp. 296–303, 2018.

[5] V. Patel, W. Li, G. Wang, F. Wang, A. Vairis, and P. Niu, "Friction stir welding of dissimilar aluminum alloy combinations: state-of-the-art," *Metals (Basel).*, vol. 9, no. 3, p. 270, 2019.

[6] T. Sathish, S. D. Kumar, K. Muthukumar, and S. Karthick, "Natural inspiration technique for the parameter optimization of A-GTAW welding of naval steel," *Mater. Today Proc.*, vol. 21, pp. 843–846, 2020.

[7] P. P. Thakur and A. N. Chapgaon, "A review on effects of GTAW process parameters on weld," *IJRASET*, vol. 4, no. 1, pp. 136–140, 2016.

[8] K. C. Sunhare, S. D. Patle, and H. K. Narang, "Optimizing TIG welding parameters for enhanced weld quality in P-91 steel," *J. Inst. Eng. Ser. D*, pp. 1–18, 2025.

[9] S. C. Moi, P. K. Pal, A. Bandyopadhyay, and R. Rudrapati, "Effect of Heat Input on the Mechanical and Metallurgical Characteristics of TIG Welded Joints.," *J. Mech. Eng.*, vol. 16, no. 2, 2019.

[10] I. Bunaziv, A. J. Tomstad, G. Kvam-Langelandsvik, and M. Eriksson, "A through-process modelling approach of aluminium heat-affected zone softening and weld joint performance," *Int. J. Adv. Manuf. Technol.*, vol. 137, no. 7, pp. 4011–4022, 2025.

[11] S. A. Rizvi and M. Ahamad, "Effect of heat input on the microstructure and mechanical properties of a Welded joint-A Review," *Int. J. Appl. Eng. Res.*, vol. 13, no. 6, pp. 184–188, 2018.

[12] L. O. Osoba, W. A. Ayoola, Q. A. Adegbuji, and O. A. Ajibade, "Influence of heat inputs on weld profiles and mechanical properties of carbon and stainless steel," *Niger. J. Technol. Dev.*, vol. 18, no. 2, pp. 135–143, 2021.

[13] D. K. Dwivedi, "Design of Welded Joints: Weld Bead Geometry: Selection, Welding Parameters," in *Fundamentals of Metal Joining: Processes, Mechanism and Performance*, Springer, 2021, pp. 343–351.

[14] A. Gradoboev, I. Matveeva, D. Ryabov, R. Vakhromov, V. Mann, and A. Krokhin, "Influence of the Mg/Si Ratio on Speed Extrusion of 6XXX Alloys," in *Light Metals 2022*, Springer, 2022, pp. 322–328.

[15] Z. Sui *et al.*, "Effect of aging treatment on microstructure and mechanical properties of as-extruded AA6063 aluminum alloy," *J. Mater. Eng. Perform.*, vol. 34, no. 7, pp. 5506–5516, 2025.

[16] S. L. Rajaseelan and S. Kumarasamy, "Mechanical properties and microstructural characterization of dissimilar friction stir welded AA5083 and AA6061 aluminium alloys," *Mechanics*, vol. 26, no. 6, pp. 545–552, 2020.

[17] A. Bansal, S. C. Vettivel, and M. Kumar, "Influence of activated flux on the mechanical and

microstructural response of cold metal transfer welded AA6063-MgAZ31B dissimilar alloy," *Weld. World*, vol. 69, no. 9, pp. 2745–2766, 2025.

[18] F. Njock Bayock, P. Kah, P. Layus, and V. Karkhin, "Numerical and experimental investigation of the heat input effect on the mechanical properties and microstructure of dissimilar weld joints of 690-MPa QT and TMCP steel," *Metals (Basel).*, vol. 9, no. 3, p. 355, 2019.

[19] S. Kuryntsev, "A review: laser welding of dissimilar materials (Al/Fe, Al/Ti, Al/Cu)—methods and techniques, microstructure and properties," *Materials (Basel).*, vol. 15, no. 1, p. 122, 2021.

[20] L. A. Pinto, L. Quintino, R. M. Miranda, and P. Carr, "Laser welding of dissimilar aluminium alloys with filler materials," *Weld. World*, vol. 54, no. 11, pp. R333–R341, 2010.

[21] S. Omprakasam, R. Raghu, R. Sudhakar, and M. P. Saravanan, "Comprehensive investigation of microstructural evolution, mechanical behavior, and corrosion resistance in TIG welded AA7075 alloy with ER4043 filler," *J. Mech. Sci. Technol.*, vol. 39, no. 7, pp. 4121–4127, 2025.

[22] S. F. Eshraghi, M. H. Farshidianfar, S. F. Nabavi, S. Marandi, and A. Farshidianfar, "The Effect of Fusion Zone Oxygen Content and Weld Geometry on Hardness and Porosity of Laser-Welded CP Titanium Sheets," *Lasers Manuf. Mater. Process.*, vol. 12, no. 2, pp. 346–368, 2025.

[23] A. Gupta *et al.*, "Optimization of welding strength in the tungsten inert gas welding process for aluminium alloys," *Front. Mech. Eng.*, vol. 11, p. 1569059, 2025.

[24] J. Prakash, S. P. Tewari, and B. K. Srivastava, "Shielding gas for welding of aluminium alloys by TIG/MIG welding-a review," *Mod. Eng. Res.*, vol. 1, no. 2, pp. 690–699, 2011.

[25] S. Boczkal *et al.*, "Analysis of the Structure and Properties of Welded Joints Made from Aluminum Alloys by Electron Beam Welding (EBW) and Friction Stir Welding (FSW)," *Crystals*, vol. 15, no. 3, p. 208, 2025.

[26] Y. Sun, Z. Zhou, C. Li, L. Yu, and Y. Liu, "Precipitates evolution and strengthening of Al–Mg2Si alloys containing high-Cu contents during ageing process," *J. Mater. Sci.*, vol. 57, no. 37, pp. 17828–17838, 2022.

[27] Q. Dong *et al.*, "Formation mechanism of layered structure near fusion boundary in dissimilar-filler welding of aluminum alloys," *Metall. Mater. Trans. A*, vol. 52, no. 4, pp. 1174–1179, 2021.

[28] K. Karthick, K. Sravanthi, S. P. Jani, D. A. Prabu, S. V. T, and H. L. Allasi, "Optimization of TIG welding parameters and filler rod material selection for dissimilar aluminum alloy joints," *J. Mater. Sci. Mater. Eng.*, vol. 20, no. 1, p. 80, 2025.

[29] B. Alzahrani, M. M. Z. Ahmed, M. I. A. Habba, R. A. Fouad, Y. G. Y. Elshaghoul, and E. A. Gadallah, "Tig welding of EN AW-6082 Al alloy: a comparative analysis of filler rods on microstructural and mechanical performance," *J. Manuf. Mater. Process.*, vol. 9, no. 1, p. 21, 2025.

[30] A. Khalfallah, M. Moradi, and R. Beygi, "Welding and joining of metallic materials: microstructure and mechanical properties," 2024, *MDPI*.

[31] M. Shafeek, S. Suranjan, D. Doreswamy, and H. K. Sachidananda, "Effect of welding parameters on microstructure and mechanical properties of GMAW welded S275 steel welded zone," *Discov. Mater.*, vol. 4, no. 1, p. 96, 2024.

[32] G. Dak and C. Pandey, "Study on effect of weld groove geometry on mechanical behavior and residual stresses variation in dissimilar welds of P92/SS304L steel for USC boilers," *Arch. Civ. Mech. Eng.*, vol. 22, no. 3, p. 140, 2022.

[33] J. Yang *et al.*, “The Influence of Predefined Grooves on the Gas Tungsten Arc Welding Performance of 7072 Aluminum Alloy,” *J. Mater. Eng. Perform.*, vol. 34, no. 16, pp. 17460–17471, 2025.
[34] A. Deschamps, “Microstructural Evolution in Heat-Treatable Aluminum Alloys,” *Encycl. Therm. Stress.*, pp. 3027–3041, 2014.
[35] I. S. Zuiko, S. Malopheyev, S. Rahimi, S. Mironov, and R. Kaibyshev, “The evolution of abnormal grains during the heating stage of a post-weld solution treatment in a friction-stir-welded 2519 aluminium alloy,” *Metals (Basel).*, vol. 13, no. 6, p. 1033, 2023.
[36] P. Shahsavari and H. R. Rezaei Ashtiani, “Effects of preheating and cooling rate on the microstructure and mechanical properties of tungsten inert gas welded joints of AA5083-H321 aluminum alloy,” *J. Mater. Eng. Perform.*, vol. 29, no. 10, pp. 6790–6801, 2020.
[37] W. Guo, X. Zhao, Y. Zhao, Y. Liu, H. Li, and B. Han, “Research on optimal heat input parameter for TIG welding of thin plate 5083 aluminum alloy,” *Sci. Rep.*, vol. 15, no. 1, p. 15593, 2025.
[38] R. Bendikiene, A. Jutas, and A. Ciuplys, “Evaluation of hardness variation in 5754-H111 aluminium TIG welds under thermal/straining effects: role of AC and DC welding pre-/post-deformation,” *Int. J. Adv. Manuf. Technol.*, vol. 138, no. 11, pp. 5945–5958, 2025.

Received: June 19, 2026
Accepted: August 02, 2026